RESEARCH ARTICLE

Sub-millimetre resolution laminar fMRI using Arterial Spin Labelling in humans at 7 T

Sriranga Kashyap[1,2]☯*, **Dimo Ivanov**[1,2]☯*, **Martin Havlicek**[1], **Laurentius Huber**[1,2],
Benedikt A. Poser[1,2], **Kâmil Uludağ**[3,4,5]

1 Department of Cognitive Neuroscience, Faculty of Psychology and Neuroscience, Maastricht University, Maastricht, The Netherlands, **2** Maastricht Brain Imaging Centre (M-BIC), Maastricht University, Maastricht, The Netherlands, **3** Center for Neuroscience Imaging Research, Institute for Basic Science, Sungkyunkwan University, Suwon, South Korea, **4** Department of Biomedical Engineering, N Center, Sungkyunkwan University, Suwon, South Korea, **5** Techna Institute & Koerner Scientist in MR Imaging, University Health Network, Toronto, Canada

☯ These authors contributed equally to this work.
* sriranga.kashyap@maastrichtuniversity.nl (SK); dimo.ivanov@maastrichtuniversity.nl (DI)

Abstract

Laminar fMRI at ultra-high magnetic field strength is typically carried out using the Blood Oxygenation Level-Dependent (BOLD) contrast. Despite its unrivalled sensitivity to detecting activation, the BOLD contrast is limited in its spatial specificity due to signals stemming from intra-cortical ascending and pial veins. Alternatively, regional changes in perfusion (i.e., cerebral blood flow through tissue) are colocalised to neuronal activation, which can be non-invasively measured using Arterial Spin Labelling (ASL) MRI. In addition, ASL provides a quantitative marker of neuronal activation in terms of perfusion signal, which is simultaneously acquired along with the BOLD signal. However, ASL for laminar imaging is challenging due to the lower SNR of the perfusion signal and higher RF power deposition i.e., specific absorption rate (SAR) of ASL sequences. In the present study, we present for the first time in humans, isotropic sub-millimetre spatial resolution functional perfusion images using Flow-sensitive Alternating Inversion Recovery (FAIR) ASL with a 3D-EPI readout at 7 T. We show that robust statistical activation maps can be obtained with perfusion-weighting in a single session. We observed the characteristic BOLD amplitude increase towards the superficial laminae, and, in apparent discrepancy, the relative perfusion profile shows a decrease of the amplitude and the absolute perfusion profile a much smaller increase towards the cortical surface. Considering the draining vein effect on the BOLD signal using model-based spatial "convolution", we show that the empirically measured perfusion and BOLD profiles are, in fact, consistent with each other. This study demonstrates that laminar perfusion fMRI in humans is feasible at 7 T and that caution must be exercised when interpreting BOLD signal laminar profiles as direct representation of the cortical distribution of neuronal activity.

🔓 OPEN ACCESS

Introduction

Neuronal activity in the brain is associated with an increased metabolic demand accompanied by changes in haemodynamics such as blood oxygenation, flow and volume (for reviews see [1–4]). Functional magnetic resonance imaging (fMRI) is a technique that can non-invasively measure these changes and allows inferring the spatial pattern of neuronal activity while performing a task or at rest. Improvements in MRI technology over the past decades, such as higher magnetic field strengths, novel sequences, optimised pulse designs, and parallel imaging, have pushed the spatial and temporal limits to an extent wherein MRI at ultra-high magnetic field (UHF, ≥ 7 T) can routinely achieve sub-millimetre spatial resolution voxels in humans, for both structural and functional imaging (see Special Issues [5, 6] and reviews therein). While fMRI investigations have yielded robust, reproducible functional parcellation [7] of different brain areas consistent with previous ex vivo cyto- and myelo-architectural studies [8, 9], the advantages of UHF fMRI have enabled neuroscientists to investigate the mesoscopic circuitry within regions across cortical depths and, to a lesser extent, columns in humans (see Special Issue [10] and reviews therein). A vast majority of standard-resolution and laminar fMRI studies have been performed using the Blood Oxygenation Level-Dependent (BOLD) contrast [11, 12]. While the BOLD contrast excels in its sensitivity to detect signal changes due to its high signal-to-noise (SNR), it is inherently limited in its spatial specificity relative to site of neuronal activation because of strong signal bias introduced via the intra-cortical ascending veins [13] and by the non-local signal spread (drainage effect) through pial veins [14, 15]. Studies investigating the specificity of the laminar BOLD response in humans and animals [16–20] have consistently observed the largest signal change in the BOLD signal at the superficial layers and pial surface despite the fact that the peak of the neuronal activity is expected in the input layers (layer IV in human V1) for feed-forward stimuli [21, 22]. Some earlier studies have investigated the leakage of the signal between laminae during steady-state [22–24]. Recently, a fully dynamical model of the laminar BOLD signal has been developed [13] that enables model-driven 'deconvolution' (i.e. removal of the intra-cortical ascending venous signal) of the measured BOLD signal profiles to unravel the underlying neuronally-driven signal profiles. However, theoretical assumptions of these model-driven approaches have not yet been subjected to experimental validation. The versatility of MRI provides the means to also measure other (non-BOLD) haemodynamic response parameters such as cerebral blood volume (CBV) using vascular space occupancy (VASO) [25–27] or cerebral blood flow (CBF) through tissue (perfusion) using arterial spin labelling (ASL) [28–30]. Most studies using these non-BOLD approaches have been carried out in animal models [1, 31, 32] and have only been applied to high-resolution human studies with the advent of UHF fMRI [33–35]. From the perspective of laminar fMRI, animal studies have shown that perfusion-weighting is a highly desirable contrast, even more so than total CBV, due to its spatial proximity to neuronal activation [18, 36]. While CBV-weighted imaging using VASO has seen a resurgence for laminar fMRI applications [37], perfusion-weighted fMRI using ASL has been mostly limited to relatively low spatial resolution ($\approx$ 2-4 mm) studies [38] (but see [39]). Achieving higher spatial resolutions, let alone sub-millimetre resolution, with perfusion-weighting and adequate brain coverage is challenging. This is due to the relatively lower SNR of the perfusion-weighted signal owing to the lower microvascular density relative to tissue volume ($\approx$ 1-2%) and T_1 recovery of the labelled arterial water signal, and the higher RF power deposition of ASL sequences in general. The SNR limitation can be addressed to some extent by moving to UHF. The gain in SNR due to increased field strength [40] and the prolonged longitudinal relaxation times (T_1) [41, 42] allows longer post-labelling delays, thereby, improving the perfusion SNR [34]. Recent developments using ASL at 7 T [34, 35, 43–45] have

enabled pushing the spatial resolution for perfusion-mapping to the sub-millimetre regime [46, 47] by overcoming several technical challenges; i.e. optimisation of sequence and pulse design [33, 35, 45, 48], using dielectric pads [49, 50] in order to improve the labelling efficiency [34], and the utilisation of a 3D-EPI readout [51]. Taking together the advantages of UHF, the spatial specificity of the perfusion signal and the fact that ASL acquires both BOLD and perfusion-weighted images simultaneously, makes ASL a very attractive tool for laminar fMRI. In the present study, we build on our previous work [46, 47] to acquire, for the first time, sub-millimetre resolution simultaneous BOLD and perfusion-weighted fMRI of the human visual cortex at 7 T. We demonstrate that robust, participant-specific, single-session, high-resolution perfusion activation maps can be obtained for laminar fMRI in humans at 7 T. We probe the cortical depth-dependence of BOLD and perfusion-weighted signals in response to visual stimulation in humans and reconcile our experimental findings using the recently proposed dynamic model of the laminar BOLD signal.

Materials and methods

Seven healthy volunteers (median age = 28 years) participated in the study following screening and having given written informed consent. The study was approved by the Ethics Review Committee for Psychology and Neuroscience (ERCPN) at Maastricht University and all procedures followed the principles expressed in the Declaration of Helsinki.

Data acquisition

Data were acquired on a whole-body Siemens Magnetom 7 T research scanner with a gradient system capable of maximum gradient amplitude of 70 mT/m and maximum slew rate of 200 T/m/s (Siemens Healthineers, Erlangen, Germany) and a 32-channel receive phased array head coil (Nova Medical, USA). The participant placement and preparatory procedure followed the protocol previously described in [34, 43]. In short, the eye centres were taken as iso-centre reference (instead of the eyebrows, as is typically done) and supplementary cushions were provided to the participants under the neck, to ensure that the large feeding arteries to the brain were parallel to the B_0. In addition, two 18x18x0.5 cm^3 high-permittivity dielectric pads containing a 2.8:1 solution of calcium titanate ($CaTiO_3$) and heavy water (D_2O) by weight [52] were placed on either side of the head at the level of the participant's temporal lobes to increase B_1+ (therefore, labelling) efficiency at 7 T [50]. This was done because our earlier work [34, 43] found that the relative orientation of large feeding arteries together with the use of dielectric pads gave the best perfusion results.

Stimulus paradigm. Full contrast black-and-white radial flickering checkerboard was presented using PsychoPy v1.90.0 [53] for 20 s (stimulus on) followed by 40 s of an iso-luminant grey background (stimulus off). Each functional run was ≈ 11 min long consisting of a 30 s initial baseline period and ten stimulus on-off blocks. The participants were instructed to remain motionless and fixate on a central fixation dot throughout each of the four functional runs.

Anatomical MRI. Anatomical data were acquired using a 3D-MP2RAGE [54] at 0.9 mm isotropic spatial resolution (192 sagittal slices; GRAPPA = 3; FoV_{read} = 230 mm; phase-encoding = A-P; TI_1/TI_2 = 900/2750 ms; a_1/a_2 = 5˚/3˚; TE/TR = 2.39/4500 ms; partial-Fourier$_{phase}$ = 6/8; bandwidth = 250 Hz/px; echo-spacing = 6.6 ms, TA = 6 min).

Functional MRI. Functional data were acquired at a nominal resolution of 0.9 mm isotropic using a pulsed ASL (PASL) sequence [29] with a 3D-EPI readout [51] segmented along the second phase-encoding direction with each k-space plane acquired with a single-shot, and a Flow-sensitive Alternating Inversion Recovery (FAIR) [55] Quantitative Imaging of Perfusion

using a Single Subtraction, second version (QUIPSS II) [30] labelling scheme (44 axial slices; GRAPPA = 4; FoV$_{read}$ = 192 mm; phase-encoding = A-P; TE/TR = 15/2850 ms; a = 19˚; TI$_1$/TI$_2$ = 700/1891 ms; partial-Fourier$_{phase}$ = 5/8; partial-Fourier$_{slice}$ = 7/8; Ref. lines PE = 64; Ref. scan mode = FLASH [56]; bandwidth = 1124 Hz/px; echo-spacing = 1.02 ms, repetitions = 230, TA = 11 min). The flip angle was chosen so that the M$_{xy}$ signal is constant across segments. The nominal point spread function (PSF) for these acquisition parameters was simulated and is shown in S1 Fig. The FWHM of the PSF along the phase-encoding direction was estimated to be 2 voxels. To minimise this blurring due to the use of partial-Fourier [57], all the ASL data were reconstructed using a GRAPPA kernel size of {3,2} [43] and 8 iterations of the POCS algorithm [58, 59] as implemented by Siemens. The labelling was achieved using a Time Resampled Frequency Offset Corrected Inversion (TR-FOCI) pulse [48] (10 ms) that provided efficient (up to 95%) slab-selective inversion despite inhomogeneous B$_1$ and SAR constraints at high field [34, 37] (S2 Fig). Immediately after each of the four functional runs, five volumes with opposite phase-encoding were acquired for run-wise distortion-correction. The functional data acquisition slab was oriented to cover as much of the occipital lobe as possible in all participants centred on the calcarine sulcus (S3a Fig).

Data processing

The anatomical data were pre-processed in SPM12 r7487 (https://www.fil.ion.ucl.ac.uk/spm/software/spm12) [60, 61] and FSL v6.0 (https://fsl.fmrib.ox.ac.uk/fsl/fslwiki) [62, 63] using the workflow illustrated in S4 Fig. This anatomical pre-processing workflow was developed particularly to work well for MP2RAGE data (https://github.com/srikash/presurfer). First, the second inversion image of the MP2RAGE was subjected to the automated segmentation in SPM12 [64]. The bias-corrected second inversion image was used to create a whole-brain mask using FSL BET [65]. The thresholded non-brain tissue classes from the SPM12 segmentation were summed together to create a mask of the non-brain tissue and large sinuses. The non-brain mask was manually curated in cases, in which the automatic masks were sub-optimal. The T$_1$-weighted MP2RAGE image (UNI) was bias-corrected using SPM12 and was stripped off the non-brain tissue and large sinuses using the mask obtained from the second inversion image. This pre-processed T$_1$-weighted MP2RAGE was supplied as input to the high-resolution recon-all pipeline of Freesurfer v6.0 (https://surfer.nmr.mgh.harvard.edu) [66]. Additionally, the MP2RAGE T$_1$ map was supplied as an additional input (proxy T$_2$-weighted image) for pial surface optimisation. The segmentation and surface construction were done in the native resolution and the segmentation quality in the occipital lobe was manually curated (S5 Fig). A probabilistic retinotopic atlas was applied to the Freesurfer reconstructed data using *neuropythy* (https://github.com/noahbenson/neuropythy) [67] to obtain participant-specific V1 and V2 regions-of-interest (ROIs) (S3b Fig). Following the automatic segmentation and reconstruction, the WM surface was extended into WM by 30% of the cortical thickness to account for any discrepancy of the GM-WM boundary when using T$_1$-weighted MP2RAGE images [68]. The first inversion image of the MP2RAGE was used to check the extended WM boundaries due to its sharp WM-GM contrast. We also extended the pial boundary by the same amount into the CSF to sample the signal away from the pial boundary. Then, we generated a total of twenty-one intermediate equi-volume surfaces within the GM using Surface tools (https://github.com/kwagstyl/surface_tools) [69] (S3c Fig). The functional datasets were pre-processed using Advanced Normalization Tools (ANTs) v2.3.1 (https://github.com/ANTsX/ANTs) [70, 71]. First, the functional runs were subjected to affine realignment. Next, the temporal mean of the functional run and the

temporal mean of the opposite phase-encoded run were used to calculate an undistorted template image and the distortion-correction warps were saved. Lastly, a transformation matrix was calculated for each functional run to the T_1-weighted data using the visual alignment tools in ITK-SNAP v3.6 [72] and a final rigid alignment using ANTs. All transforms were concatenated and applied to the unprocessed functional datasets in a single resampling step using a 4th degree B-spline interpolation. This minimises resolution losses due to multiple interpolation steps while providing the required quality of registration accuracy in laminar fMRI studies [73, 74]. Statistical analyses of the functional data were carried out using the 'Full Perfusion Signal Modelling' pipeline [75] in FSL FEAT [76, 77]. Here, we modelled three regressors i.e., the stimulus design convolved with the canonical haemodynamic response function (HRF) representing the BOLD signal, the alternating label-control acquisition of the ASL sequence representing the baseline perfusion-weighting and the combination of these two regressors representing the perfusion activation [78, 79]. Due to the disparity in the spatial spreads of the BOLD and perfusion activation (Fig 2 left panel), a mask of the overlap between the BOLD and perfusion activation cluster thresholded masks from FEAT was created. This ensured that we sampled the BOLD and perfusion signals from the same voxels. Laminar analyses were carried out in Freesurfer by sampling the functional time-series signal from the ROIs using nearest-neighbour interpolation. No surface or intra-cortical smoothing was applied. The laminar time-courses sampled from V1 and V2 across all participants were imported into MATLAB R2016b (MathWorks, USA) for the time-series analyses. The BOLD and perfusion-weighted time-courses were obtained for each lamina by applying surround-averaging and surround-subtraction, respectively [80–82] and the event-related average time-courses were calculated. The event-related average BOLD time-course was subsequently rescaled to percent BOLD signal change relative to the pre-stimulus baseline ($\approx$10 s). The analysis of the perfusion time-series followed several steps: First, the perfusion-weighted time-series is a measure of the modulation depth (i.e., the magnitude of the zig-zag) of the raw ASL time-course in MRI signal units (S6 Fig). It is important to note that these data are not scaled in physiological units and is representative of the perfusion SNR of the data. We then derived the following measures from perfusion-weighted time-course: absolute and relative perfusion change, and baseline perfusion. Absolute perfusion change was calculated by taking the change in the perfusion activation (i.e., by subtracting the pre-stimulus baseline) per lamina and then normalising the signal with the mean of the EPI (to account for transmit-receive biases and baseline T_2^* effects). The absolute perfusion change, thus obtained, is in arbitrary units but proportional to the quantitative perfusion change. The absolute perfusion change can then be rescaled into physiological units, as typically done in perfusion quantification studies [38, 83]. Relative perfusion change is the percentage change in the perfusion signal due to activation per depth relative to its respective baseline. Note that the relative perfusion change does not need to be divided by the mean EPI image for scaling (as it appears both in the numerator and the denominator and thus cancels out). The baseline perfusion (Fig 1a) was calculated using simple subtraction of the label-control time-points during the baseline period ($\approx$ 0-30 s at the beginning of the run) and pre-stimulus intervals ($\approx$ 0-10 s before stimulus onset) of the stimulus blocks. The temporal signal-to-noise of the perfusion-weighted timeseries (perfusion tSNR) image (Fig 1b) was calculated as the ratio of the temporal mean to the temporal standard deviation of the perfusion-weighted timeseries. Laminar steady-state profiles of the BOLD signal, absolute and relative perfusion change signals were calculated by averaging the respective signals within the $\approx$ 14-28 s interval following stimulus onset. The baseline perfusion laminar profile (S7 Fig) was obtained by averaging within the entire ROI.
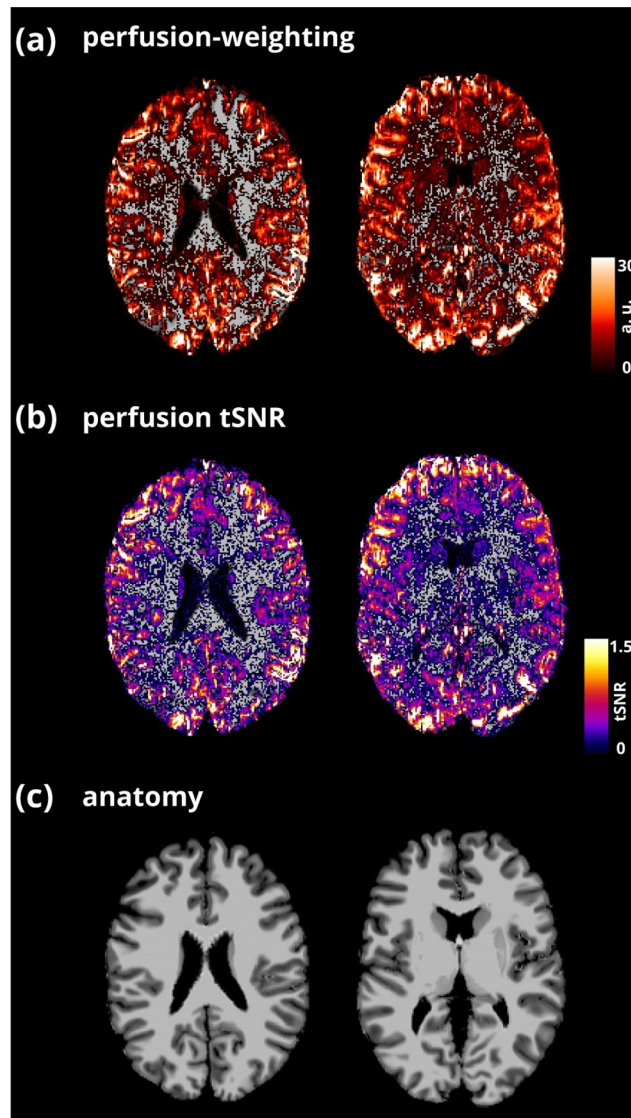
Fig 1. The average baseline perfusion (a) and perfusion tSNR (b) maps from a superior (left) and inferior (right) slice of an example participant is shown overlaid on the corresponding T_1-weighted anatomical image (c).

https://doi.org/10.1371/journal.pone.0250504.g001

Simulating the laminar BOLD signal from the measured perfusion profile

The experimentally measured laminar BOLD response profiles in V1 and V2 regions were compared to theoretical predictions of the dynamical laminar BOLD signal model of Havlicek and Uludag [13] using their publicly available MATLAB code (https://github.com/martinhavlicek/laminar_BOLD_model). In order to do this, some assumptions regarding baseline physiological parameters were made. That is, the laminar BOLD signal profile is fully determined given physiological values and measured CBF changes. These assumptions are within typical values of human vascular physiology (see [4] for a review, and references therein). Here, the measured absolute perfusion laminar profiles (both baseline and activation) were used to input the physiological parameters of the model. The total amount of venous baseline CBV (CBV_0) was set to 2 mL, of which 50% relates to microvasculature (ω_v=0.5) and
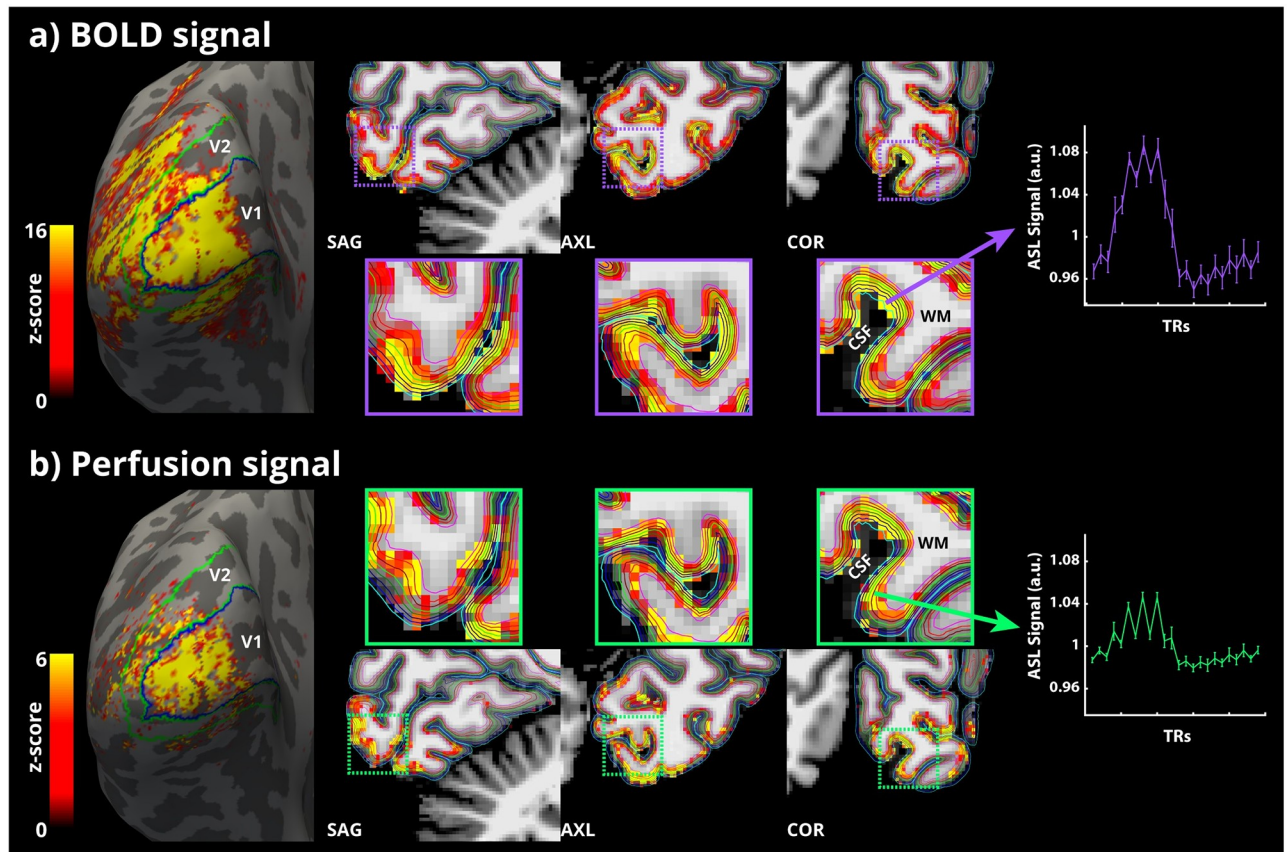
Fig 2. (a, left-right) BOLD signal activation map of an example participant, averaged over all runs, overlaid on the inflated left hemisphere reconstruction from Freesurfer. Contours of the V1 (blue) and V2 (green) labels obtained from Neuropythy are also overlaid on the inflated surface. Cropped orthogonal views of the participant's occipital lobe with the BOLD signal activation map overlaid in voxel space. Boundaries of the different laminar surfaces are also overlaid, colour-coded from cyan (pial)-to-magenta (white). The purple dotted square inset indicates the zoomed-out views presented below. Event-related average ASL time-course of highly BOLD activated voxels across runs for this participant is shown to the right. (b, left-right) The same are presented for perfusion activation in green. The error-bars indicate SEM across trials.

50% to the ascending veins (ω_d = 0.5) [84]. The baseline CBV (CBV_0) distribution was set to be constant across laminae in the microvasculature but increased linearly towards the surface in the ascending veins (slope, s_d = 0.4). Since the baseline perfusion (CBF_0) obtained from the ASL data was not in physiological units of mL/min/100 g, we rescaled the CBF_0 by a constant scaling factor x=5520 calculated using the following assumptions. First, that the CBV_0 in microvasculature (1 mL /100 g) is divided uniformly between all laminae and the mean transit time (t_{v0}) through microvasculature (averaged across all laminae) is 1 s (for complete list of other model parameters, see Table 2 in [13]), giving an average CBF_0 of 1 mL/s/100 g or 60 mL/min/100 g. This scaling factor allows a rescaling of the CBF from arbitrary MRI units to physiologically meaningful units for the purpose of reporting. However, the laminar BOLD model itself is driven by depth-dependent changes in relative CBF (in %), therefore, the exactness of the scaling in physiological units is not critical to the simulations. Next, by assuming a linear coupling between CBF and O_2 metabolism, depth-dependent changes in microvasculature $CMRO_2$ were obtained (n = 3) [85]. We also assume relative CBV changes in microvasculature and ascending veins are related to the relative CBF via Grubb exponents α_v = 0.35 and α_d = 0.1, respectively [86, 87]. Finally, we assume that 65% of the O_2 is extracted on arrival at the venules (E_0=0.35) with no further extraction along these vessels (i.e., O_2 saturation of

haemoglobin ($1-E_0$) is assumed to be homogeneously distributed across laminae). All other parameters were defined as in the default scenario described in [13]. Please note that we did not fit the model to data but used experimentally obtained perfusion-weighted signal data and plausible biophysical parameters to generate a prediction of the laminar BOLD signal profile.

Results

Baseline perfusion

Fig 1a and 1b show two representative slices (one superior, one inferior) of the average baseline perfusion map and the perfusion temporal signal-to-noise (tSNR) of a participant overlaid on the T_1-weighted anatomical image (Fig 1c). These maps show that the average perfusion signal is highly localised to the GM ribbon and demonstrates the quality of the co-registration between the acquisition slab with the anatomy as indicated by the absence of signal shifted into the ventricles and the clearly defined sulci (wherever resolvable). The perfusion-weighted data shown in Fig 1a is in arbitrary MRI signal units.

Functional activation

Robust statistical activation was obtained for all participants for both the BOLD (Fig 2a) and perfusion signals (Fig 2b). The BOLD activation envelopes a much larger swath of cortex than perfusion activation does (Fig 2, left panel). This is expected given the differences in the detection sensitivity (i.e. functional contrast-to-noise (fCNR)) between the BOLD and perfusion signals, and the presence of BOLD signal in pial veins. In addition, the BOLD activation obtained follows the characteristic localisation pattern observed with standard GE-EPI studies. That is, the largest BOLD activated voxels are always localised at the CSF-GM boundary (Fig 2a, purple zoomed-out boxes). In contrast, the perfusion activation was observed to be more spatially localised to the GM ribbon with the highest activated voxels localised mid- to deep-GM (Fig 2b, green zoomed-out boxes). The activation maps are shown in the three orthogonal views to highlight the consistency of the GM localisation of activation in 3D.

Finally, the ASL time-courses exhibit a zig-zag modulation that is characteristic of ASL sequences (due to the acquisition of alternating label and control volumes) demonstrating the high quality of the data. The modulation depth of this zig-zag represents the amount of labelled spins delivered to the tissue and is, therefore, proportional to tissue perfusion. The ASL time-course obtained from the highest BOLD signal activated voxels in grey matter shows the typically observed increase in the BOLD signal magnitude during activation with weaker zig-zag modulation (Fig 2a, right panel, purple). On the other hand, the ASL time-course obtained from the highest perfusion-activated voxels shows the strong zig-zag modulation throughout but with lower BOLD signal modulation (Fig 2b, right panel, green). Please note, that the zig-zag time-courses represent the event-related average response over all depths of grey matter from the ASL timeseries. All three key differences between the BOLD and perfusion activation signals were consistently observed in all the participants.

Laminar analysis

The group-average laminar time-courses of BOLD signal change, absolute perfusion change, and relative perfusion change are shown in Fig 3 for V1 and in Fig 4 for V2. The temporal behaviour of the three sampled signals across all laminae is presented as a heat-map in the top row with time along the X-axis, the cortical depth along the Y-axis, and the magnitude of the signal in colour code. We observed inter-regional differences with laminar responses of all three signals, with V2 having a lower amplitude than V1. The laminar profiles of the BOLD
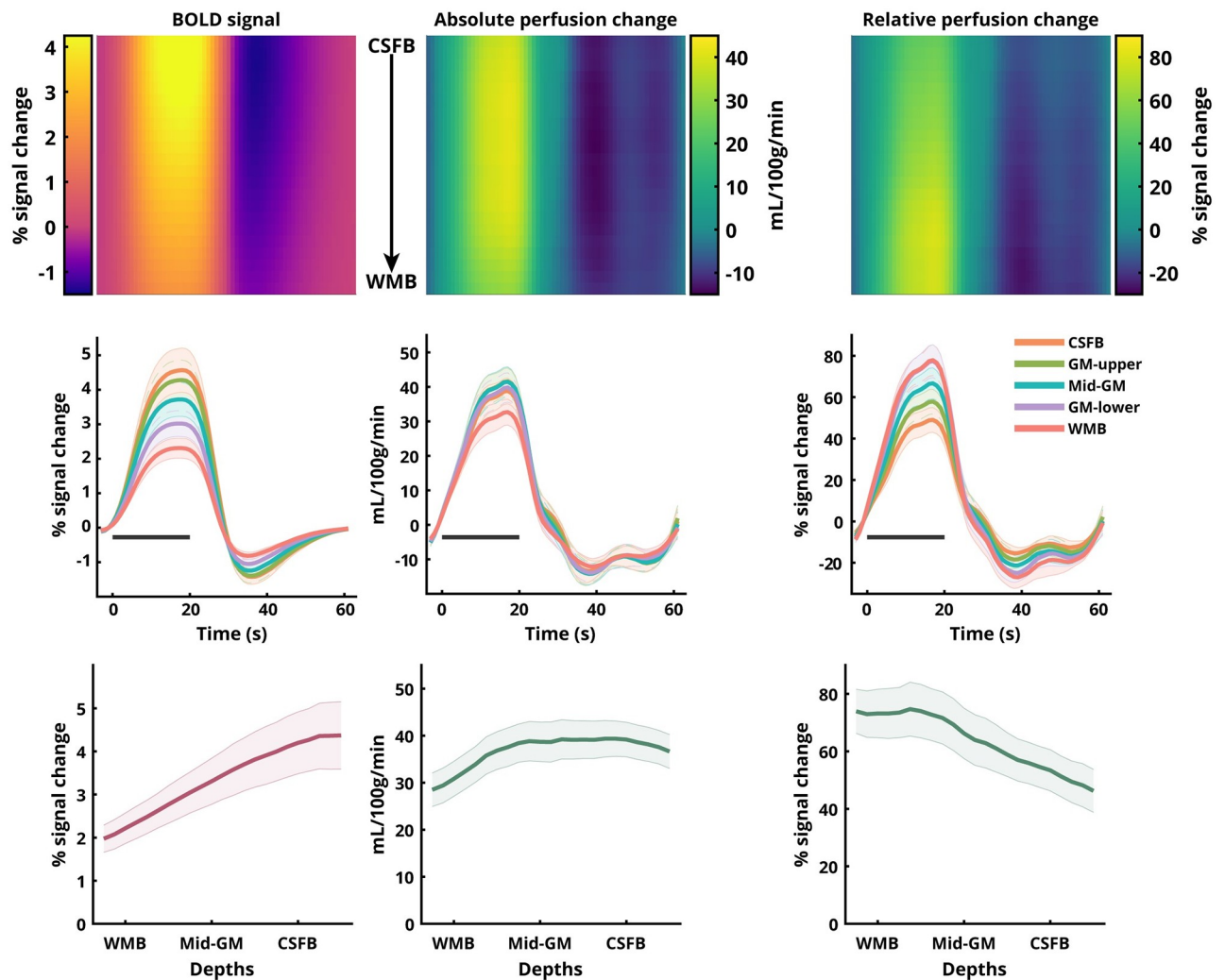
Fig 3. Laminar BOLD and perfusion signal changes in human V1 ROI obtained using sub-millimetre 3D-EPI ASL at 7 T. Top row: Heat-map representations of the group-average BOLD signal change, absolute perfusion change, and relative perfusion change with cortical depth along Y-axis and time along the X-axis. Middle row: Five out of the twenty-three total laminar time-courses for the respective sampled signals. Bottom row: Laminar profiles of the positive response during stimulation for the respective sampled signals with cortical depth along X-axis. Error-bars indicate SEM across participants. The black bar in the middle row indicates the stimulus duration.

signal change exhibit positive slopes (Slope V1: 4.88 ± 0.129, Slope V2: 4.81 ± 0.195) with a strong linear trend (R^2 V1: 0.986, R^2 V2: 0.967). The laminar profiles of the relative perfusion change, on the other hand, exhibit negative slopes (Slope V1: -4.91 ± 0.27, Slope V2: -4.64 ± 0.111) with a strong linear trend (R^2 V1: 0.939, R^2 V2: 0.988). Interestingly, the absolute perfusion changes exhibit a moderately positive slope (Slope V1: 3.35 ± 0.68, Slope V2: 3.80 ± 0.485) albeit without a strong linear trend (R^2 V1: 0.537, R^2 V2: 0.745). In the perfusion signals, slight oscillatory behaviour is observed during the post-stimulus period.

Simulations of the laminar BOLD signal

Fig 5 shows the simulated laminar BOLD signal profile (solid blue lines) and the experimentally measured laminar BOLD signal profiles (dotted purple lines, see Figs 3 and 4). The measured and simulated profiles were highly congruent (Pearson's correlation: r = 0.9984 for V1,
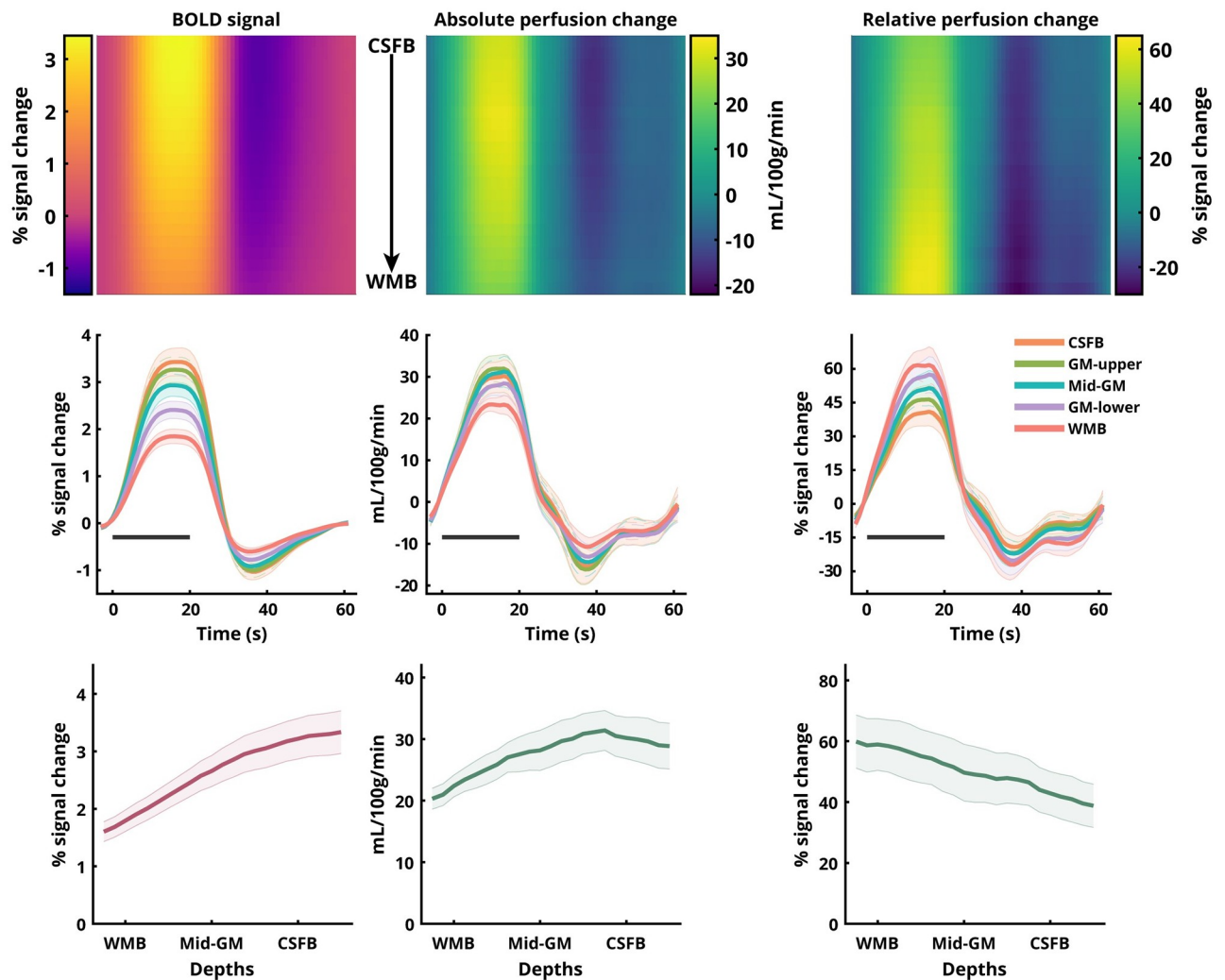
Fig 4. Same as Fig 3 for V2 ROI.

r = 0.9977 for V2), demonstrating that, despite the discrepancy of the relative and absolute perfusion, and the BOLD signal profiles, they are in fact compatible with each other.

Discussion

The present study, is the first demonstration in humans of the improved spatial specificity of the perfusion signal compared to the BOLD signal using isotropic sub-millimetre spatial resolution ASL at 7 T. We found incongruent cortical depth profiles between the BOLD signal and perfusion changes, which, however, turned out to be physiologically consistent with each other after employing a dynamical BOLD signal model.

Functional BOLD and perfusion activation

We obtained robust participant-specific, single-session activation maps for simultaneously acquired isotropic sub-millimetre spatial resolution BOLD and perfusion signals at 7 T. We observed a larger spread of activation for the BOLD signal (Fig 2a) compared to the perfusion signal (Fig 2b). This is expected because the detection sensitivity of the perfusion signal
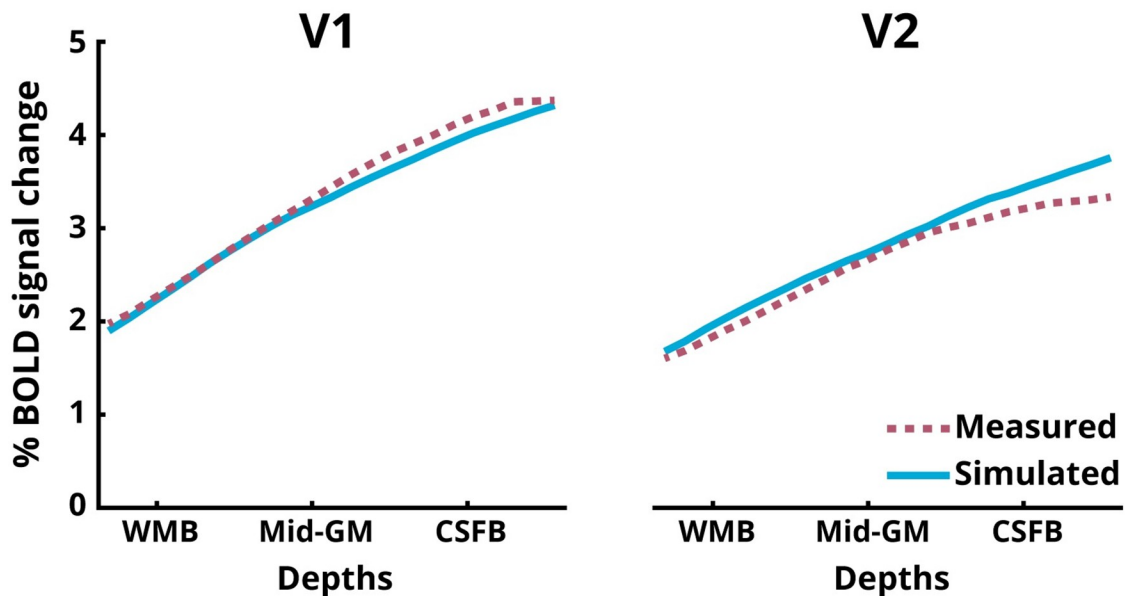
Fig 5. Laminar profiles of the BOLD signal for V1 and V2 ROIs. The measured responses are the same as the BOLD signal profiles in Figs 3 and 4. The simulated profiles are obtained using the laminar BOLD model proposed in [13] (S7 Fig).

(fCNR) is much lower than that of the BOLD signal [34, 38, 39]. Additionally, this can also be explained by the higher spatial specificity of the perfusion signal compared to the BOLD signal, which is susceptible to non-local signal spread due to downstream venous bias away from the actual site of activation [15, 88]. This is also observed in high-resolution fMRI with the highest BOLD activated voxels located at the CSF-GM boundary (Fig 2a). On the other hand, the perfusion activation map exhibits a well-defined localisation to the cortical ribbon (Fig 2b), mostly located in cortical GM [18]. Importantly, given that perfusion signal has much lower fCNR than the BOLD signal in standard resolution studies (2-4 mm in each direction), it was not necessarily expected that ASL will have enough sensitivity at sub-millimetre resolution for detecting perfusion activation. One reason that with increasing resolution there is enough perfusion fCNR is that, not only image SNR, but also partial voluming with CSF and WM is decreased, i.e., thermal, and physiological noise coming from outside GM are reduced. This is different for the BOLD signal as pial vessels located in CSF (see Fig 2a) do contribute to the overall BOLD signal in low resolution studies and therefore, increases in spatial resolution decrease both image SNR and overall signal contribution. That is, going from low- to high-spatial resolution penalizes CNR of the BOLD signal more than of the perfusion signal. Recently, a novel fMRI approach called VAPER [89] has also been put forward as a contrast useful for perfusion-weighted high-resolution fMRI by mixing VASO and perfusion contrasts. Although the combination of two contrasts boosts VAPER's sensitivity, it markedly complicates its ability to quantify perfusion and also, its physiological specificity. Thus, established ASL techniques remain the most feasible way to acquire in vivo perfusion-weighted images that can be straightforwardly validated using quantitative fMRI models, and can be expected to provide reproducible results across a wide range of sequence parameters and field strengths [34]. While the present study employs a PASL acquisition scheme, recent studies have explored the feasibility of using a pCASL acquisition scheme with a 3D-GRASE readout for perfusion-weighted laminar fMRI at 7T in the motor cortex [90, 91]. While the PASL laminar profile seems consistent with that of the present study, the pCASL profile shows a relatively higher

baseline perfusion in the middle layers. The measured profiles are the outcome of a complex interplay between one or more of several factors such as readout approach, background suppression scheme, partial voluming, post-stimulus inhibitions in certain layers, residual pial arterial contributions despite long transit times [92]. The sources of this apparent discrepancy observed with the labelling schemes and their interplay with other ASL parameters (e.g., TE, spatial resolution, selection of voxels, labelling schemes and timings, background suppression etc.) needs further investigation. At this moment, there is very little in vivo data in terms of a full exploration of the impact of the parameter space that ASL offers for laminar fMRI. Thus, having demonstrated the feasibility of perfusion-weighted laminar fMRI at 7 T, future studies can consider systematic comparisons of the different labelling approaches, readout strategies and how they affect the laminar profiles of perfusion both during baseline and activation at UHF. A recent review used an exemplary dataset from the current study to illustrate the potential of perfusion-weighted imaging in the context of exciting avenues for non-BOLD laminar fMRI applications at UHF [93]. As highlighted in the review, the perfusion contrast has been highly desired for laminar fMRI as the perfusion signal is relatively unaffected by the venous compartments, both by the pial and ascending veins, and the large arterial compartments. In comparison, the BOLD signal is heavily weighted towards the venous compartments and the VASO signal can have contributions from both arterial and venous in addition to CBV changes in microvasculature [33, 94, 95]. The reason for the high perfusion localisation specificity is that the tagged arterial water is mostly exchanged with the tissue at the level of the capillaries. In addition, the transit delay for the labelled blood to arrive at the region-of-interest (in this case, occipital lobe) can be $\approx$1-1.3 s [96]. Together with the blood transit time within tissue on the order of $\approx$1-2.5 s [97], only little longitudinal magnetisation of the tag remains (due to T_1 decay), i.e. that almost no magnetisation of the label is present in venous blood (see S8 Fig), except for artefacts caused by labelling of venous blood superior to the imaging slab in some ASL schemes (see [83]). The transit time for the acquisition in the present study was optimised for the visual cortex [92], and is reflected in the inter-regional differences in the baseline perfusion signal and its temporal stability of the tissue (Fig 1). The absence of the venous bias and the signal being dominated by the capillary compartment implies that the perfusion contrast more closely follows both the spatial profile and the amplitude of cortical metabolism and neuronal activation. Another important aspect of ASL acquisitions is the possibility to obtain a quantitative estimate of the baseline signal across depths. The difference between the highly BOLD-activated or highly perfusion-activated voxels is readily visible in the ASL time-courses (Fig 2). The time-courses for perfusion activation show reduced amplitude of the signal envelope and larger difference between pairs of data points (i.e., the zig-zag modulation) indicating that these voxels contain signals from mostly the microvasculature and that observed responses are indeed capturing the changes in perfusion. In contrast, there are small zig-zag changes relative to the overall signal envelope in the time-courses for the highest BOLD activation, reflecting a smaller contribution from microvasculature. This means that the spatial non-overlap that we observe between the perfusion and BOLD signals is driven largely by differences in the underlying physiology and not the differences in SNR.

Laminar BOLD and perfusion responses

We replicated previous findings [21, 73, 98] that the event-related average BOLD signal amplitude (Figs 3 and 4, first column) increases towards the CSF-GM boundary (e.g., [99, 100]). The BOLD signal increase to the superficial layers is well understood and can be attributed to two signal biases: (a) increase in baseline CBV of the intra-cortical ascending veins, and (b) the non-local blooming effect from the pial veins ([101], and for overview see, [4]). The presence

of these biases in the BOLD signal makes the interpretation of the measured laminar signal profile, specifically in the superficial layers, challenging [102]. One approach to deal with the issue of spatial bias in GE-BOLD signal is model-driven spatial 'deconvolution' [22, 24], which, however, has not yet been validated with another (simultaneously) acquired fMRI modality. The profile of the relative perfusion change (Figs 3 and 4, right column) exhibits the opposite behaviour (compared to the BOLD profile) [103] with the magnitude of the signal increasing towards the GM-WM boundary with a strong linear trend. Furthermore, QUIPSS II pulses were employed in the present study allowing clear-cut definition of the tagged bolus. This means that the observed patterns of laminar signal behaviour are unlikely to be due to undelivered tagged blood in the diving arterioles. Although the impact of the QUIPSS II pulse depends on the chosen parameters and the arrival times to the regions-of-interest, an increase in blood flow upon activation can result in a more complete delivery of the tagged spins to the tissue, including the deeper layers at the time of volume acquisition. This could yield a larger fractional perfusion change in the deeper layers relative to the baseline condition. While it is usually argued that for feed-forward stimuli the peak in activation must be in the middle layers, electrophysiological evidence, histology, and a previous BOLD signal study after spatial 'deconvolution' [22] support the view that V1 also receives increased input signal into layer VI in addition to layer IV. Please note that despite the high spatial resolution used in this study, we could not detect a fine-grained distinction between laminae. The perfusion spatial profile obtained, thus, represents a smoothed version of the underlying neuronal activity. For example, data shown in Fig 4b and 4d in [22] and in [104] (see Fig 9 in [22]) are compatible with the spatial profiles found in the current study. We find that the relative increase in the perfusion signal in the middle to deeper layers is also consistent with animal literature (see also [18, 105, 106]). The absolute perfusion signal change profile (Figs 3 and 4, middle column) exhibits a weak positive slope and non-linear behaviour across depths. However, both relative and absolute signal changes are derived from the same perfusion-weighted signal obtained after surround-subtraction and the difference stems from the spatial profile of the baseline perfusion (S5 Fig). Please note, that the increase of the absolute perfusion signal from WMB to CSFB (by ≈ 30-50%) is much smaller than that of the BOLD signal (by ≈ 100-120%). Additionally, in contrast to the BOLD signal, the absolute perfusion change drops beyond the CSF border. It is important to reiterate that the perfusion and BOLD signals were extracted from the exact same patch of cortex using a mask of the spatial overlap between the BOLD and perfusion activations. This was done due to the larger significantly activated volume using the BOLD compared to the perfusion contrast. By adopting this approach, we show that despite having the same underlying cortical architecture, the relative and absolute perfusion signal changes differ in their depth-dependent behaviour and both differ from the BOLD signal either in the sign of their slope or the relative increase of the profile towards the surface. Here, the BOLD signal profile obtained from ASL is consistent with profiles from previous studies acquiring GE-BOLD signal alone. In order to test if the apparent discrepancy between the relative and absolute perfusion profiles and BOLD profile can be reconciled, we simulated the BOLD signal profile from the measured perfusion profiles using the recent dynamical laminar BOLD signal model (for details, see S7 Fig). We show that the positive slope and the relative increase of the measured BOLD profile can be obtained from the laminar profile of the relative (having negative slope) and absolute (having much smaller increase towards the surface) perfusion signal by modelling the ascending vein bias, i.e., simulating the laminar BOLD response in a forward manner. Therefore, we conclude that despite their seemingly contrasting behaviours, the BOLD and perfusion signal profiles are, in fact, physiologically consistent with each other. Additionally, the BOLD time-courses exhibit a strong post-stimulus undershoot (PSU) consistent with previous studies [73, 107]. Interestingly, our perfusion measures also exhibit PSUs

but with smaller amplitudes relative to the positive response. In contrast to the smooth recovery of the PSU to baseline in the BOLD signal, the perfusion PSU exhibits slight oscillatory behaviour. These post-stimulus oscillatory transients are consistent with previous reports of perfusion measurements in humans (e.g., [108]) and with optical imaging in rodents [109]. The oscillatory transients observed in the previous perfusion study in humans [108] could not resolve any depth-dependent modulations owing to its much lower spatial resolution (i.e. 2.65 x 2.65 x 5 mm^3). The post-stimulus oscillations in our study near the WM boundary are smoother and evolve with a different oscillatory phase than near the CSF boundary, where the oscillations are more pronounced (Figs 3 and 4, middle panels). While this observation in itself is interesting, pin-pointing the exact vascular physiology that elicits this behaviour is beyond the scope of this study. Taken together, we believe that the current study presents a breakthrough in non-BOLD fMRI research with the development of sub-millimetre resolution perfusion fMRI using ASL and its feasibility for layer-specific investigations, which has hitherto been an uncharted territory in humans.

Data processing

We developed a novel workflow to pre-process anatomical images (S4 Fig) by using the second inversion image of the MP2RAGE and SPM12's segmentation to automatically mask out the sagittal and transverse sinuses that are crucial for highly accurate pial surface delineation using Freesurfer's recon-all. In some participants, the workflow required (albeit very little) manual corrections of the segmentation masks (S5 Fig). We used an open-source python package, *neuropythy* [67], to apply a probabilistic atlas of retinotopy in participant's native space to generate automatic labels of V1 and V2 (S3b Fig). We qualitatively compared this atlas-based approach on a separate dataset of pRF mapping that was acquired using the same scanner, head coil and similar coverage, and found a high degree of overlap consistent with the findings of [67]. Please note, the focus of the present work is distinguishing the BOLD and perfusion signals, and does not rely on the perfect delineation of V1 and V2 borders. Cortical layering was done using the equi-volume approach [110] using Surface tools [111] as equi-volumetric layering is currently not natively supported in Freesurfer. Even though the layering is done on the whole cortical ribbon, we manually ensured that the delineations were accurate within the V1 and V2 masks in each participant. Nevertheless, for spatial resolutions such as the present study, the exact choices of the layering model [112] and the number of sampled depths [101] does not affect our main conclusions. As ASL measures the BOLD signal simultaneously with perfusion, the BOLD signal profile serves as an internal control and can be compared to other BOLD signal only studies, and the perfusion profile is compared to the BOLD signal profile that is concurrently acquired. The BOLD signal spatial profile for feed-forward stimuli (such as checkerboards used in this study) is well known and the BOLD signal derived from the ASL data reproduces this well-known amplitude increase towards the surface of the cortex (Figs 3 and 4), confirming the accuracy of the data processing. It is important to note that the TE in the present study was 15 ms owing to the EPI readout, and allowed us to minimise BOLD weighting of the acquisition. Furthermore, we obtained our perfusion-weighted timeseries using the surround-subtraction approach which has been demonstrated previously [80, 82] to significantly reduce BOLD contamination in the perfusion-weighted timeseries. We additionally calibrated the perfusion-weighted data using the mean EPI image in order to correct for any residual baseline T_2^* effects. While minimal processing approaches for fMRI have been proposed [113], except for a few studies (such as [37, 73, 99, 114–116]), they are unfortunately not commonplace in laminar fMRI. We once again highlight the importance of minimal processing, and demonstrate its feasibility using the ANTs framework to estimate, combine and apply

transformations of motion, distortion-correction and co-registration to the anatomical image in a single resampling step, thereby reducing the amount of smoothing resulting from the processing of the data [74]. Please note, in some ASL acquisitions there may be strong differences in image contrast between the label and control images, and the choice of realignment cost-function may impact the quality of correction. However, this was not the case for the present study (S9 Fig). Importantly, as can be seen in Fig 2, high values of perfusion were tightly confined to the GM ribbon illustrating the high accuracy of the segmentation and co-registration in the present study.

Limitations

The goal of the present study was to demonstrate the feasibility of using perfusion-weighted contrast with ASL for laminar fMRI and, to that end, we employed a block design with a strong feed-forward visual stimulus that is known to elicit widespread activation. Due to the lower SNR of the perfusion-signal, we averaged approximately 44 min worth of functional data. While there is the undoubted benefit in spatial specificity, ASL may not be well-suited for all laminar fMRI studies, particularly those with small effect sizes. In addition, GE-BOLD laminar fMRI data are routinely acquired with 0.6-0.8 mm isotropic resolutions, higher than the current ASL study. While the use of partial-Fourier acquisition [117] can reduce the effective spatial resolution along a dimension, the amount of blurring was reduced by using 8 iterations of the POCS reconstruction algorithm [59] instead of the default zero-filling [57]. At 7 T, large-coverage high-resolution single-TR acquisitions are unfeasible without substantial acceleration. Thus, a combination of GRAPPA 4 and phase partial-Fourier was used to shorten the echo time and gain perfusion SNR. The partial-Fourier in the slice direction may cause some SNR loss compared to an image with fully sampled slice dimension. The reason for the partial-Fourier sampling in the slice direction is to ensure optimal TI2 for the k-space centre and an adequate TR. Having the concurrently acquired BOLD signal information as an internal control, we do not expect this to have affected our main findings in the present study. We expect that any of the limitations from the partial-Fourier factors employed are offset by the gain in perfusion SNR (and CNR) due to the shorter TE. The lowest achievable TE in the present study was 15 ms owing to the EPI readout, which is still not ideally suited for perfusion imaging. It would be desirable to achieve even shorter TEs (e.g. $\approx$3 ms or less) for better perfusion-weighting, however it is currently not possible using conventional Cartesian EPI readouts. To this end, there has been recent progress in non-Cartesian (e.g. spiral readouts) ASL fMRI at ultra-high field [118, 119]. Dual-echo spiral acquisitions can be particularly useful for simultaneous perfusion and BOLD imaging achieving the first echo at $\approx$2 ms (perfusion-weighted) and the second echo at $\approx$25 ms (BOLD) at 7 T. However, these non-Cartesian acquisitions are prone to inaccuracies in the spiral trajectories due to gradient imperfections that require real-time monitoring and correction using specialised field-monitoring hardware [118]. However, research and development are still underway to address these technical challenges in non-Cartesian imaging and currently sub-millimetre fMRI acquisitions have not been demonstrated. Nevertheless, to the best of our knowledge, this study remains the highest spatial resolution functional ASL study in humans till date. Going forward, sub-millimetre resolution ASL can be invaluable to studies that are examining BOLD signal physiology, for validating existing models or for brain areas contaminated by close large pial veins. Future development work in both acquisition and reconstruction can push the boundaries of spatial and temporal resolutions of ASL for laminar fMRI at ultra-high fields. We show that high-resolution ASL at ultra-high field is possible using the standard commercial head-coil with single-channel transmit (NOVA Medical, USA). However, the B_1+ inhomogeneities remain a major hurdle [34].

While we were able to mitigate this to some extent using dielectric pads [50, 52], future studies will be able to take advantage of advances in parallel transmission (pTx) technology [120] or the use of dedicated labelling-only RF-coils [121–124] to potentially further optimise high-resolution ASL fMRI at ultra-high fields. Having demonstrated the feasibility of perfusion-weighted laminar fMRI using ASL at a sub-millimetre spatial resolution, future studies will be able to systematically evaluate different properties ASL and its impact on the perfusion signal evolution at ultra-high fields.

Supporting information

S1 Fig. Point spread function of the 3D-EPI acquisition along the principal phase encoding and readout directions. Partial-Fourier [117] was employed along the principal phase encoding direction. Please note, this simulation used zero-filling with partial-Fourier representing the default image reconstruction scenario. However, in the present study, a POCS reconstruction [59] with 8 iterations was carried out which minimises partial-Fourier blurring, and consequently improves the PSF [57].
(TIF)

S2 Fig. (a) The red outlines are the segmented arteries using a separate time-of-flight (ToF) scan and segmented using *braincharter* (https://github.com/braincharter/vasculature) [125]. (b) The B_1+ map is overlaid on the second inversion image of the MP2RAGE with the arteries overlaid as white outline. At the point of the cross-hair (internal carotid artery), the B_1+ value is measured to be 7.85 μT in this participant, which is in line with the 95% inversion efficiency threshold for our TR-FOCI pulse. Therefore, the arterial water spins in the feeding vessels are adequately labelled in the present study.
(TIF)

S3 Fig. Illustration of (a) the extent and orientation of the acquisition slab (b) the atlas-based delineation of the V1 and V2 ROIs (c) a subset of all laminar surfaces overlaid on one hemisphere.
(TIF)

S4 Fig. Anatomical data pre-processing workflow for MP2RAGE data for input to Freesurfer's recon-all (https://github.com/srikash/presurfer). Tissue classes C3-C5 were thresholded on a subject-by-subject basis to include as much of the sagittal and transverse sinuses as possible. In most of our subjects, this procedure did not require any manual correction of the combined mask. ITK-SNAP v3.6 [72] was used to make any manual corrections when required. The Freesurfer T_1-weighted input is presented as a 3D render showing an intact GM surface at the occipital lobe with the green arrows indicating locations of the now automatically stripped sagittal and transverse sinuses.
(TIF)

S5 Fig. (top) Coronal view of the pial surface overlaid on a standard skull-stripped T_1-weighted MP2RAGE image. Shown in red is determined from the standard HiRes workflow and in yellow is determined from the optimised workflow shown in S4 Fig. White dotted lines indicate sagittal sinus and cyan arrows emphasise the erroneous placement of the pial surface in the standard workflow. (bottom) Sagittal views of the pial surface from the standard and optimised workflows to further illustrate their differences in outcome indicated by the cyan arrows.
(TIF)

S6 Fig. Laminar profile of the perfusion-weighted signal (obtained after surround-subtraction) in human V1 and V2 from the sub-millimetre 3D-EPI ASL at 7 T. (top row) Heatmap representations of the group-average perfusion-weighted signal with cortical depth along Y-axis and Time along the X-axis. (middle row) Five out of the twenty-three total laminar time-courses and (bottom row) laminar profiles of the positive response for the perfusion-weighted signal. All error-bars indicate SEM. The grey bar in the middle row indicates the stimulus duration.
(TIF)

S7 Fig. (left-to-right) Measured absolute perfusion signal for activation and baseline, relative perfusion laminar profile obtained from measured absolute perfusion data, assumed laminar baseline blood volume, and comparison of measured BOLD signal change and simulated BOLD signal change as predicted by the dynamical laminar BOLD model [13].
(TIF)

S8 Fig. Event-related average ASL time-course sampled from the pial veins near the V1 ROI. Error bars indicate SEM across trials. Please note the near absence of the characteristic ASL zig-zag signal modulation and the small scale of the Y-axis (in MRI signal units).
(TIF)

S9 Fig. Temporal mean EPI image of all control (a) and label (b) volumes from a single ASL run.
(TIF)

S10 Fig. (left-to-right) Single-subject and average laminar profiles of the positive response during stimulation for the BOLD signal, absolute and relative perfusion change with cortical depth along the X-axis.
(TIF)

Acknowledgments

Author Contributions

Conceptualization: Sriranga Kashyap, Dimo Ivanov, Kâmil Uludağ.

Data curation: Sriranga Kashyap, Dimo Ivanov.

Formal analysis: Sriranga Kashyap, Martin Havlicek.

Funding acquisition: Kâmil Uludağ.

Methodology: Sriranga Kashyap, Dimo Ivanov, Martin Havlicek, Laurentius Huber, Benedikt A. Poser, Kâmil Uludağ.

Resources: Dimo Ivanov, Kâmil Uludağ.

Software: Sriranga Kashyap, Dimo Ivanov, Martin Havlicek, Laurentius Huber, Benedikt A. Poser.

Supervision: Kâmil Uludağ.

Validation: Dimo Ivanov.

Visualization: Sriranga Kashyap.

Writing – original draft: Sriranga Kashyap, Martin Havlicek, Kâmil Uludağ.

Writing – review & editing: Sriranga Kashyap, Dimo Ivanov, Laurentius Huber, Benedikt A. Poser, Kâmil Uludağ.

References

1. Goense J, Whittingstall K, Logothetis NK. Neural and BOLD responses across the brain. Wiley Inter-discip Rev Cogn Sci. 2012; 3(1):75–86. https://doi.org/10.1002/wcs.153

2. Kim SG, Ogawa S. Biophysical and physiological origins of blood oxygenation level-dependent fMRI signals. Journal of Cerebral Blood Flow and Metabolism. 2012; 32(7):1188–1206. https://doi.org/10.1038/jcbfm.2012.23

3. Logothetis NK, Wandell BA. Interpreting the BOLD Signal. Annu Rev Physiol. 2004; 66(1):735–769. https://doi.org/10.1146/annurev.physiol.66.082602.092845

4. Uludag K, Blinder P. Linking brain vascular physiology to hemodynamic response in ultra-high field MRI. NeuroImage. 2018; 168:279–295. https://doi.org/10.1016/j.neuroimage.2017.02.063

5. Polimeni JR, Uludag K, editors. Neuroimaging with ultra-high field MRI: Present and future. Elsevier; 2018. Available from: https://www.sciencedirect.com/journal/neuroimage/vol/168/.

6. Yacoub E, Wald LL, editors. Pushing the spatio-temporal limits of MRI and fMRI. Elsevier; 2018. Available from: https://www.sciencedirect.com/journal/neuroimage/vol/164/.

7. Glasser MF, Coalson TS, Robinson EC, Hacker CD, Harwell J, Yacoub E, et al. A multi-modal parcel-lation of human cerebral cortex. Nature. 2016; 536(7615):171–178. https://doi.org/10.1038/nature18933 PMID: 27437579

8. Brodmann K. Vergleichende Lokalisationslehre der Grosshirnrinde in ihren Prinzipien dargestellt auf Grund des Zellenbaues. J.A. Barth; 1909.

9. Vogt O. Die myeloarchitektonische Felderung des menschlichen Stirnhirns. J.A. Barth; 1910. Available from: https://books.google.nl/books?id=5DFkQwAACAAJ.

10. Polimeni JR, Norris DG, editors. MRI of Cortical Layers. Elsevier; 2019. Available from: https://www.sciencedirect.com/journal/neuroimage/special-issue/105LWQPR49Q.

11. Ogawa S, Lee TM, Kay AR, Tank DW. Brain magnetic resonance imaging with contrast dependent on blood oxygenation. Proceedings of the National academy of Sciences of the United States of America. 1990; 87(24):9868–9872. https://doi.org/10.1073/pnas.87.24.9868

12. Ogawa S, Tank DW, Menon R, Ellermann JM, Kim SG, Merkle H, et al. Intrinsic signal changes accompanying sensory stimulation: functional brain mapping with magnetic resonance imaging. Pro-ceedings of the National academy of Sciences of the United States of America. 1992; 89(13):5951–5955. https://doi.org/10.1073/pnas.89.13.5951 PMID: 1631079

13. Havlicek M, Uludag K. A dynamical model of the laminar BOLD response. NeuroImage. 2020; 204:609099. https://doi.org/10.1016/j.neuroimage.2019.116209

14. Lai S, Hopkins AL, Haacke EM, Li D, Wasserman BA, Buckley P, et al. Identification of vascular struc-tures as a major source of signal contrast in high resolution 2D and 3D functional activation imaging of the motor cortex at l.5T preliminary results. Magnetic Resonance in Medicine. 1993; 30(3):387–392. https://doi.org/10.1002/mrm.1910300318 PMID: 8412613

15. Turner R. How much cortex can a vein drain? Downstream dilution of activation-related cerebral blood oxygenation changes. NeuroImage. 2002; 16(4):1062–1067. https://doi.org/10.1006/nimg.2002.1082

16. Chen G, Wang F, Gore JC, Roe AW. Layer-specific BOLD activation in awake monkey V1 revealed by ultra-high spatial resolution functional magnetic resonance imaging. Neuroimage. 2013; 64(1):147–155. https://doi.org/10.1016/j.neuroimage.2012.08.060

17. Harel N, Lin J, Moeller S, Ugurbil K, Yacoub E. Combined imaging-histological study of cortical laminar specificity of fMRI signals. Neuroimage. 2006; 29(3):879–887. https://doi.org/10.1016/j.neuroimage.2005.08.016

18. Jin T, Kim SG. Cortical layer-dependent dynamic blood oxygenation, cerebral blood flow and cerebral blood volume responses during visual stimulation. Neuroimage. 2008; 43(1):1–9. https://doi.org/10.1016/j.neuroimage.2008.06.029

19. Zhao F, Jin T, Wang P, Kim SG. Improved spatial localization of post-stimulus BOLD undershoot rela-tive to positive BOLD. Neuroimage. 2007; 34(3):1084–1092. https://doi.org/10.1016/j.neuroimage.2006.10.016

20. Zhao F, Wang P, Kim SG. Cortical depth-dependent gradient-echo and spin-echo BOLD fMRI at 9.4T. Magnetic Resonance in Medicine. 2004; 51(3):518–524. https://doi.org/10.1002/mrm.10720

21. Koopmans PJ, Barth M, Orzada S, Norris DG. Multi-echo fMRI of the cortical laminae in humans at 7T. Neuroimage. 2011; 56(3):1276–1285. https://doi.org/10.1016/j.neuroimage.2011.02.042

22. Marquardt I, Schneider M, Gulban OF, Ivanov D, Uludag K. Cortical depth profiles of luminance contrast responses in human V1 and V2 using 7 T fMRI. Hum Brain Mapp. 2018;. https://doi.org/10.1002/hbm.24042

23. Heinzle J, Koopmans PJ, den Ouden HEM, Raman S, Stephan KE. A hemodynamic model for layered BOLD signals. Neuroimage. 2016; 125:556–570. https://doi.org/10.1016/j.neuroimage.2015.10.025

24. Markuerkiaga I, Barth M, Norris DG. A cortical vascular model for examining the specificity of the laminar BOLD signal. Neuroimage. 2016; 132:491–498. https://doi.org/10.1016/j.neuroimage.2016.02.073

25. Donahue MJ, Lu H, Jones CK, Edden RAE, Pekar JJ, van Zijl PCM. Theoretical and experimental investigation of the VASO contrast mechanism. Magnetic resonance in medicine. 2006; 56(6):1261–1273. https://doi.org/10.1002/mrm.21072

26. Jin T, Kim SG. Improved cortical-layer specificity of vascular space occupancy fMRI with slab inversion relative to spin-echo BOLD at 9.4 T. NeuroImage. 2008; 40:59–67. https://doi.org/10.1016/j.neuroimage.2007.11.045

27. Lu H, Golay X, Pekar JJ, Van Zijl PC. Functional magnetic resonance imaging based on changes in vascular space occupancy. Magnetic Resonance in Medicine. 2003; 50(2):263–274. https://doi.org/10.1002/mrm.10519

28. Detre JA, Leigh JS, Williams DS, Koretsky AP. Perfusion imaging. Magnetic Resonance in Medicine. 1992; 23(1):37–45. https://doi.org/10.1002/mrm.1910230106

29. Kwong KK, Chesler DA, Weisskoff RM, Donahue KM, Davis TL, Ostergaard L, et al. MR perfusion studies with T1-weighted echo planar imaging. Magnetic Resonance in Medicine. 1995; 34(6):878–887. https://doi.org/10.1002/mrm.1910340613 PMID: 8598815

30. Wong EC, Buxton RB, Frank LR. Quantitative imaging of perfusion using a single subtraction (QUIPSS and QUIPSS II). Magnetic resonance in medicine. 1998; 39(5):702–708. https://doi.org/10.1002/mrm.1910390506

31. Fukuda M, Poplawsky AJ, Kim SG. Submillimeter-resolution fMRI: Toward understanding local neural processing. vol. 225. Elsevier; 2016. Available from: http://dx.doi.org/10.1016/bs.pbr.2016.03.003.

32. Kim SG. Biophysics of BOLD fMRI investigated with animal models. Journal of Magnetic Resonance. 2018; 292:82–89. https://doi.org/10.1016/j.jmr.2018.04.006

33. Huber L, Ivanov D, Krieger SN, Streicher MN, Mildner T, Poser BA, et al. Slab-selective, BOLD-corrected VASO at 7 Tesla provides measures of cerebral blood volume reactivity with high signal-to-noise ratio. Magnetic Resonance in Medicine. 2014; 72(1):137–148. https://doi.org/10.1002/mrm.24916 PMID: 23963641

34. Ivanov D, Gardumi A, Haast RAM, Pfeuffer J, Poser BA, Uludag K. Comparison of 3 T and 7 T ASL techniques for concurrent functional perfusion and BOLD studies. NeuroImage. 2017; 156:363–376. https://doi.org/10.1016/j.neuroimage.2017.05.038

35. Pfeuffer J, Adriany G, Shmuel A, Yacoub E, Van De Moortele PF, Hu X, et al. Perfusion-based high-resolution functional imaging in the human brain at 7 Tesla. Magnetic Resonance in Medicine. 2002; 47(5):903–911. https://doi.org/10.1002/mrm.10154 PMID: 11979569

36. Goense J, Bohraus Y, Logothetis NK. fMRI at High Spatial Resolution: Implications for BOLD-Models. Frontiers in Computational Neuroscience. 2016; 10:66. https://doi.org/10.3389/fncom.2016.00066

37. Huber L, Handwerker DA, Jangraw DC, Chen G, Hall A, Stuber C, et al. High-Resolution CBV-fMRI Allows Mapping of Laminar Activity and Connectivity of Cortical Input and Output in Human M1. Neuron. 2017; 96(6):1253–1263.e7. https://doi.org/10.1016/j.neuron.2017.11.005 PMID: 29224727

38. Alsop DC, Detre JA, Golay X, Gunther M, Hendrikse J, Hernandez-Garcia L, et al. Recommended implementation of arterial spin-labeled perfusion MRI for clinical applications: A consensus of the ISMRM perfusion study group and the European consortium for ASL in dementia. Magnetic resonance in medicine. 2015; 73(1):102–116. https://doi.org/10.1002/mrm.25197 PMID: 24715426

39. Gardumi A, Ivanov D, Havlicek M, Formisano E, Uludag K. Tonotopic maps in human auditory cortex using arterial spin labeling. Human Brain Mapping. 2016;. https://doi.org/10.1002/hbm.23444 PMID: 27790786

40. Pohmann R, Speck O, Scheffler K. Signal-to-noise ratio and MR tissue parameters in human brain imaging at 3, 7, and 9.4 tesla using current receive coil arrays. Magnetic Resonance in Medicine. 2016; 75(2):801–809. https://doi.org/10.1002/mrm.25677

41. Rooney WD, Johnson G, Li X, Cohen ER, Kim SG, Ugurbil K, et al. Magnetic field and tissue dependencies of human brain longitudinal 1H2O relaxation in vivo. Magnetic resonance in medicine. 2007; 57(2):308–318. https://doi.org/10.1002/mrm.21122 PMID: 17260370

42. Wright PJ, Mougin OE, Totman JJ, Peters AM, Brookes MJ, Coxon R, et al. Water proton T1 measurements in brain tissue at 7, 3, and 1.5 T using IR-EPI, IR-TSE, and MPRAGE: results and optimization. Magma (New York, NY). 2008; 21(1–2):121–130. https://doi.org/10.1007/s10334-008-0104-8

43. Ivanov D, Poser BA, Huber L, Pfeuffer J, Uludag K. Optimization of simultaneous multislice EPI for concurrent functional perfusion and BOLD signal measurements at 7T. Magnetic Resonance in Medicine. 2016;. https://doi.org/10.1002/mrm.26351 PMID: 27465273

44. Ivanov D, Poser BA, Kashyap S, Gardumi A, Huber L, Uludag K. Sub-millimeter human brain perfusion imaging using arterial spin labelling at 3 and 7 Tesla. In: ISMRM Workshop on Ultra High Field MRI; 2016.

45. Zimmer F, O'Brien K, Bollmann S, Pfeuffer J, Heberlein K, Barth M. Pulsed arterial spin labelling at ultra-high field with a B 1 + -optimised adiabatic labelling pulse. Magma (New York, NY). 2016; 29 (3):463–473. https://doi.org/10.1007/s10334-016-0555-2

46. Ivanov D, Kashyap S, Haast RAM, Janssens S, Huber L, Poser BA, et al. Whole-brain sub-millimeter isotropic resolution cerebral blood flow map in humans. In: Proceedings of the 24th Annual Meeting of ISMRM; 2018.

47. Kashyap S, Ivanov D, Havlicek M, Poser BA, Uludag K. Laminar CBF and BOLD fMRI in the human visual cortex using arterial spin labelling at 7T; 2019. p. 609.

48. Hurley AC, Al-Radaideh A, Bai L, Aickelin U, Coxon R, Glover P, et al. Tailored RF Pulse for Magnetization Inversion at Ultrahigh Field. Magnetic Resonance in Medicine. 2010; 63(1):51–58. https://doi.org/10.1002/mrm.22167 PMID: 19859955

49. Webb AG. Dielectric materials in magnetic resonance. Concepts in Magnetic Resonance Part A. 2011; 38A(4):148–184. https://doi.org/10.1002/cmr.a.20219

50. Teeuwisse WM, Brink WM, Webb AG. Quantitative assessment of the effects of high-permittivity pads in 7 Tesla MRI of the brain. Magnetic resonance in medicine. 2012; 67(5):1285–1293. https://doi.org/10.1002/mrm.23108

51. Poser BA, Koopmans PJ, Witzel T, Wald LL, Barth M. Three dimensional echo-planar imaging at 7 Tesla. NeuroImage. 2010; 51(1):261–266. https://doi.org/10.1016/j.neuroimage.2010.01.108

52. Haines K, Smith NB, Webb AG. New high dielectric constant materials for tailoring the B1+ distribution at high magnetic fields. Journal of Magnetic Resonance. 2010; 203(2):323–327. https://doi.org/10.1016/j.jmr.2010.01.003

53. Peirce JW. PsychoPy–Psychophysics software in Python. Journal of Neuroscience Methods. 2007; 162(1–2):8–13. https://doi.org/10.1016/j.jneumeth.2006.11.017

54. Marques JP, Kober T, Krueger G, van der Zwaag W, Van de Moortele PF, Gruetter R. MP2RAGE, a self bias-field corrected sequence for improved segmentation and T1-mapping at high field. NeuroImage. 2010; 49(2):1271–1281. https://doi.org/10.1016/j.neuroimage.2009.10.002

55. Kim SG. Quantification of relative cerebral blood flow change by flow-sensitive alternating inversion recovery (FAIR) technique: Application to functional mapping. Magnetic Resonance in Medicine. 1995; 34(3):293–301. https://doi.org/10.1002/mrm.1910340303

56. Talagala SL, Sarlls JE, Liu S, Inati SJ. Improvement of temporal signal-to-noise ratio of GRAPPA accelerated echo planar imaging using a FLASH based calibration scan. Magn Reson Med. 2016; 75 (6):2362–2371. https://doi.org/10.1002/mrm.25846

57. McGibney G, Smith MR, Nichols ST, Crawley A. Quantitative evaluation of several partial fourier reconstruction algorithms used in mri. Magnetic Resonance in Medicine. 1993; 30(1):51–59. https://doi.org/10.1002/mrm.1910300109

58. Youla DC, Webb H. Image Restoration by the Method of Convex Projections: Part 1—Theory. IEEE Transactions on Medical Imaging. 1982; 1(2):81–94. https://doi.org/10.1109/TMI.1982.4307555

59. Haacke EM, Lindskog ED, Lin W. A Fast, Iterative, Partial-Fourier Technique Capable of Local Phase Recovery. Journal of Magnetic Resonance. 1991; 92(1):126–145. https://doi.org/10.1016/0022-2364(91)90253-P

60. Ashburner J. SPM: a history. Neuroimage. 2012; 62(2):791–800. https://doi.org/10.1016/j.neuroimage.2011.10.025

61. Penny WD, Friston KJ, Ashburner JT, Kiebel SJ, Nichols TE. Statistical Parametric Mapping: The Analysis of Functional Brain Images. Elsevier Science; 2011. Available from: https://books.google.nl/books?id=G_qdEsDlkp0C.

62. Jenkinson M, Beckmann CF, Behrens TEJ, Woolrich MW, Smith SM. FSL. Neuroimage. 2012; 62 (2):782–790. https://doi.org/10.1016/j.neuroimage.2011.09.015

63. Smith SM, Jenkinson M, Woolrich MW, Beckmann CF, Behrens TE, Johansen-Berg H, et al. Advances in functional and structural MR image analysis and implementation as FSL. Neuroimage. 2004; 23 Suppl 1:S208–19. https://doi.org/10.1016/j.neuroimage.2004.07.051 PMID: 15501092

64. Ashburner J, Friston KJ. Unified segmentation. Neuroimage. 2005; 26(3):839–851. https://doi.org/10.1016/j.neuroimage.2005.02.018

65. Smith SM. Fast robust automated brain extraction. Human brain mapping. 2002; 17(3):143–155. https://doi.org/10.1002/hbm.10062

66. Fischl B. FreeSurfer. Neuroimage. 2012; 62(2):774–781. https://doi.org/10.1016/j.neuroimage.2012.01.021

67. Benson NC, Winawer J. Bayesian analysis of retinotopic maps. eLife. 2018; 7:e40224. https://doi.org/10.7554/eLife.40224

68. Fujimoto K, Polimeni JR, van der Kouwe AJW, Reuter M, Kober T, Benner T, et al. Quantitative comparison of cortical surface reconstructions from MP2RAGE and multi-echo MPRAGE data at 3 and 7T. NeuroImage. 2014; 90:60–73. https://doi.org/10.1016/j.neuroimage.2013.12.012 PMID: 24345388

69. Wagstyl K, Lepage C, Bludau S, Zilles K, Fletcher PC, Amunts K, et al. Mapping Cortical Laminar Structure in the 3D BigBrain. Cerebral Cortex. 2018; 28(7):2551–2562. https://doi.org/10.1093/cercor/bhy074 PMID: 29901791

70. Avants BB, Tustison NJ, Song G, Cook PA, Klein A, Gee JC. A reproducible evaluation of ANTs similarity metric performance in brain image registration. Neuroimage. 2011; 54(3):2033–2044. https://doi.org/10.1016/j.neuroimage.2010.09.025

71. Avants BB, Tustison NJ, Wu J, Cook PA, Gee JC. An open source multivariate framework for n-tissue segmentation with evaluation on public data. Neuroinformatics. 2011; 9(4):381–400. https://doi.org/10.1007/s12021-011-9109-y

72. Yushkevich PA, Piven J, Hazlett HC, Smith RG, Ho S, Gee JC, et al. User-guided 3D active contour segmentation of anatomical structures: significantly improved efficiency and reliability. Neuroimage. 2006; 31(3):1116–1128. https://doi.org/10.1016/j.neuroimage.2006.01.015 PMID: 16545965

73. Kashyap S, Ivanov D, Havlicek M, Poser BA, Uludag K. Impact of acquisition and analysis strategies on cortical depth-dependent fMRI. NeuroImage. 2018; 168:332–344. https://doi.org/10.1016/j.neuroimage.2017.05.022

74. Polimeni JR, Renvall V, Zaretskaya N, Fischl B. Analysis strategies for high-resolution UHF-fMRI data. Neuroimage. 2018; 168:296–320. https://doi.org/10.1016/j.neuroimage.2017.04.053

75. Chappell M, MacIntosh B, Okell T. Introduction to Perfusion Quantification Using Arterial Spin Labelling. Oxford Neuroimaging Primers Series. Oxford University Press; 2018.

76. Woolrich MW, Behrens TE, Beckmann CF, Jenkinson M, Smith SM. Multilevel linear modelling for FMRI group analysis using Bayesian inference. Neuroimage. 2004; 21(4):1732–1747. https://doi.org/10.1016/j.neuroimage.2003.12.023

77. Worsley KJ. Statistical analysis of activation images. Functional MRI: An introduction to methods. 2001; 14:251–270. https://doi.org/10.1093/acprof:oso/9780192630711.003.0014

78. Mumford JA, Hernandez-Garcia L, Lee GR, Nichols TE. Estimation efficiency and statistical power in arterial spin labeling fMRI. NeuroImage. 2006; 33(1):103–114. https://doi.org/10.1016/j.neuroimage.2006.05.040

79. Hernandez-Garcia L, Jahanian H, Rowe DB. Quantitative analysis of arterial spin labeling FMRI data using a general linear model. Magnetic Resonance Imaging. 2010; 28(7):919–927. https://doi.org/10.1016/j.mri.2010.03.035

80. Aguirre GK, Detre JA, Zarahn E, Alsop DC. Experimental design and the relative sensitivity of BOLD and perfusion fMRI. Neuroimage. 2002; 15(3):488–500. https://doi.org/10.1006/nimg.2001.0990

81. Havlicek M, Roebroeck A, Friston KJ, Gardumi A, Ivanov D, Uludag K. On the importance of modeling fMRI transients when estimating effective connectivity: A dynamic causal modeling study using ASL data. NeuroImage. 2017; 155:217–233. https://doi.org/10.1016/j.neuroimage.2017.03.017

82. Liu TT, Wong EC. A signal processing model for arterial spin labeling functional MRI. NeuroImage. 2005; 24(1):207–215. https://doi.org/10.1016/j.neuroimage.2004.09.047

83. Cavusoglu M, Pfeuffer J, Ugurbil K, Uludag K. Comparison of pulsed arterial spin labeling encoding schemes and absolute perfusion quantification. Magnetic Resonance Imaging. 2009; 27(8):1039–1045. https://doi.org/10.1016/j.mri.2009.04.002

84. Weber B, Keller AL, Reichold J, Logothetis NK. The microvascular system of the striate and extrastriate visual cortex of the macaque. Cerebral Cortex. 2008; 18(10):2318–2330. https://doi.org/10.1093/cercor/bhm259

85. Buxton RB, Uludağ K, Dubowitz DJ, Liu TT. Modeling the hemodynamic response to brain activation. NeuroImage. 2004; 23(SUPPL. 1):S220–33. https://doi.org/10.1016/j.neuroimage.2004.07.013

86. Hua J, Liu P, Kim T, Donahue M, Rane S, Chen JJ, et al. MRI techniques to measure arterial and venous cerebral blood volume. NeuroImage. 2019; 187:17–31. https://doi.org/10.1016/j.neuroimage.2018.02.027 PMID: 29458187

87. Stefanovic B, Hutchinson E, Yakovleva V, Schram V, Russell JT, Belluscio L, et al. Functional reactivity of cerebral capillaries. Journal of Cerebral Blood Flow and Metabolism. 2008; 28(5):961–972. https://doi.org/10.1038/sj.jcbfm.9600590 PMID: 18059431

88. Menon RS. The great brain versus vein debate. NeuroImage. 2012; 62(2):970–4. https://doi.org/10.1016/j.neuroimage.2011.09.005

89. Chai Y, Li L, Huber L, Poser BA, Bandettini PA. Integrated VASO and perfusion contrast: A new tool for laminar functional MRI. NeuroImage. 2020; 207:116358. https://doi.org/10.1016/j.neuroimage.2019.116358

90. Shao X, Wang K, Wang JJD. 7T high-resolution arterial spin labeling reveals layer dependent cerebral blood flow. In: Proceedings of the 27th Scientific Meeting of ISMRM; 2019.

91. Shao X, Wang K, Wang JJD. In-vivo laminar CBF fMRI using high-resolution pseudo-continuous arterial spin labeling at 7T. In: Proceedings of the 28th Scientific Meeting of ISMRM; 2020.

92. Zappe AC, Pfeuffer J, Merkle H, Logothetis NK, Goense JB. The Effect of Labeling Parameters on Perfusion-Based fMRI in Nonhuman Primates. Journal of Cerebral Blood Flow and Metabolism. 2008; 28 (3):640–652. https://doi.org/10.1038/sj.jcbfm.9600564

93. Huber L, Uludag K, Moller HE. Non-BOLD contrast for laminar fMRI in humans: CBF, CBV, and CMRO2. Neuroimage. 2017;. https://doi.org/10.1016/j.neuroimage.2017.07.041 PMID: 28736310

94. Guidi M, Huber L, Lampe L, Gauthier CJ, Moller HE. Lamina-dependent calibrated BOLD response in human primary motor cortex. Neuroimage. 2016; 141:250–261. https://doi.org/10.1016/j.neuroimage.2016.06.030

95. Lu H, Hua J, van Zijl PCM. Noninvasive functional imaging of cerebral blood volume with vascular-space-occupancy (VASO) MRI. NMR in biomedicine. 2013; 26(8):932–948. https://doi.org/10.1002/nbm.2905

96. Wong EC, Buxton RB, Frank LR. Implementation of quantitative perfusion imaging techniques for functional brain mapping using pulsed arterial spin labeling. NMR in biomedicine. 1997; 10(4–5):237–249. https://doi.org/10.1002/(SICI)1099-1492(199706/08)10:4/5%3C237::AID-NBM475%3E3.0.CO;2-X

97. Wang J, Alsop DC, Song HK, Maldjian JA, Tang K, Salvucci AE, et al. Arterial transit time imaging with flow encoding arterial spin tagging (FEAST). Magnetic resonance in medicine. 2003; 50(3):599–607. https://doi.org/10.1002/mrm.10559 PMID: 12939768

98. Polimeni JR, Fischl B, Greve DN, Wald LL. Laminar analysis of 7T BOLD using an imposed spatial activation pattern in human V1. Neuroimage. 2010; 52(4):1334–1346. https://doi.org/10.1016/j.neuroimage.2010.05.005

99. Fracasso A, Luijten PR, Dumoulin SO, Petridou N. Laminar imaging of positive and negative BOLD in human visual cortex at 7T. Neuroimage. 2018;. https://doi.org/10.1016/j.neuroimage.2017.02.038 PMID: 28213112

100. De Martino F, Zimmermann J, Muckli L, Ugurbil K, Yacoub E, Goebel R. Cortical Depth Dependent Functional Responses in Humans at 7T: Improved Specificity with 3D GRASE. PLOS ONE. 2013; 8 (3):30–32. https://doi.org/10.1371/journal.pone.0060514

101. Kashyap S, Ivanov D, Havlicek M, Sengupta S, Poser BA, Uludag K. Resolving laminar activation in human V1 using ultra-high spatial resolution fMRI at 7T. Scientific Reports. 2018; 8(1). https://doi.org/10.1038/s41598-018-35333-3 PMID: 30459391

102. Yen CC, Papoti D, Silva AC. Investigating the spatiotemporal characteristics of the deoxyhemoglobin-related and deoxyhemoglobin-unrelated functional hemodynamic response across cortical layers in awake marmosets. Neuroimage. 2018; 164:121–130. https://doi.org/10.1016/j.neuroimage.2017.03.005

103. Shen Q, Ren H, Duong TQ. CBF, BOLD, CBV, and CMRO(2) fMRI signal temporal dynamics at 500-msec resolution. Journal of magnetic resonance imaging: JMRI. 2008; 27(18219630):599–606. https://doi.org/10.1002/jmri.21203

104. Tootell RB, Hamilton SL, Switkes E. Functional anatomy of macaque striate cortex. IV. Contrast and magno- parvo streams. The Journal of neuroscience. 1988; 8(5):1594–1609. https://doi.org/10.1523/JNEUROSCI.08-05-01594.1988

105. Duong TQ, Kim DS, Ugurbil K, Kim SG. Spatiotemporal dynamics of the BOLD fMRI signals: Toward mapping submillimeter cortical columns using the early negative response. Magnetic Resonance in Medicine. 2000; 44(2):231–242. https://doi.org/10.1002/1522-2594(200008)44:2%3C231::AID-MRM10%3E3.0.CO;2-T

106. Silva AC, Lee SP, Iadecola C, Kim SG. Early temporal characteristics of cerebral blood flow and deoxyhemoglobin changes during somatosensory stimulation. Journal of cerebral blood flow and metabolism. 2000; 20(1):201–206. https://doi.org/10.1097/00004647-200001000-00025

107. Siero JC, Hendrikse J, Hoogduin H, Petridou N, Luijten P, Donahue MJ. Cortical depth dependence of the BOLD initial dip and poststimulus undershoot in human visual cortex at 7 Tesla. Magnetic Resonance in Medicine. 2015; 73(6):2283–2295. https://doi.org/10.1002/mrm.25349

108. Mullinger KJ, Mayhew SD, Bagshaw AP, Bowtell R, Francis ST. Poststimulus undershoots in cerebral blood flow and BOLD fMRI responses are modulated by poststimulus neuronal activity. Proceedings of the National academy of Sciences of the United States of America. 2013; 110(33):13636–13641. https://doi.org/10.1073/pnas.1221287110

109. Berwick J, Johnston D, Jones M, Martindale J, Martin C, Kennerley AJ, et al. Fine Detail of Neurovascular Coupling Revealed by Spatiotemporal Analysis of the Hemodynamic Response to Single Whisker Stimulation in Rat Barrel Cortex. Journal of Neurophysiology. 2008; 99(2):787–798. https://doi.org/10.1152/jn.00658.2007 PMID: 18046008

110. Waehnert MD, Dinse J, Weiss M, Streicher MN, Waehnert P, Geyer S, et al. Anatomically motivated modeling of cortical laminae. Neuroimage. 2014; 93 Pt 2:210–220. https://doi.org/10.1016/j.neuroimage.2013.03.078 PMID: 23603284

111. Wagstyl K, Paquola C, Bethlehem R, Evans AC, Huth A. Equivolumetric layering for mesh surfaces; 2018. Available from: https://doi.org/10.5281/zenodo.1442584.

112. Kemper VG, De Martino F, Emmerling TC, Yacoub E, Goebel R. High resolution data analysis strategies for mesoscale human functional MRI at 7 and 9.4T. Neuroimage. 2018; 164:48–58. https://doi.org/10.1016/j.neuroimage.2017.03.058

113. Glasser MF, Sotiropoulos SN, Wilson JA, Coalson TS, Fischl B, Andersson JL, et al. The minimal preprocessing pipelines for the Human Connectome Project. NeuroImage. 2013; 80:105–124. https://doi.org/10.1016/j.neuroimage.2013.04.127 PMID: 23668970

114. Klein BP, Fracasso A, van Dijk JA, Paffen CLE, te Pas SF, Dumoulin SO. Cortical depth dependent population receptive field attraction by spatial attention in human V1. NeuroImage. 2018; 176:301–312. https://doi.org/10.1016/j.neuroimage.2018.04.055

115. Beckett AJS, Dadakova T, Townsend J, Huber L, Park S, Feinberg DA. Comparison of BOLD and CBV using 3D EPI and 3D GRASE for cortical layer functional MRI at 7 T. Magnetic Resonance in Medicine. 2020; 84(6):3128–3145. https://doi.org/10.1002/mrm.28347

116. Navarro KT, Sanchez MJ, Engel SA, Olman CA, Weldon KB. Depth-dependent functional MRI responses to chromatic and achromatic stimuli throughout V1 and V2. NeuroImage. 2021; 226:117520. https://doi.org/10.1016/j.neuroimage.2020.117520

117. Feinberg DA, Hale JD, Watts JC, Kaufman L, Mark A. Halving MR imaging time by conjugation: demonstration at 3.5 kG. Radiology. 1986; 161:527–31. https://doi.org/10.1148/radiology.161.2.3763926

118. Engel M, Kasper L, Barmet C, Schmid T, Vionnet L, Wilm B, et al. Single-shot spiral imaging at 7 T. Magnetic resonance in medicine. 2018; 80(5):1836–1846. https://doi.org/10.1002/mrm.27176 PMID: 29575161

119. Kurban D, Liberman G, Kashyap S, Ivanov D, Poser BA. Simultaneous multi-slice spiral acquisitions for CBF fMRI at 7T. In: Proceedings of the ISMRM Workshop on Ultrahigh Field Magnetic Resonance; 2019.

120. Adriany G, de Moortele PF, Wiesinger F, Moeller S, Strupp JP, Andersen P, et al. Transmit and receive transmission line arrays for 7 Tesla parallel imaging. Magnetic Resonance in Medicine. 2005; 53 (2):434–445. https://doi.org/10.1002/mrm.20321 PMID: 15678527

121. Alsaedi A, Thomas D, Bisdas S, Golay X. Overview and Critical Appraisal of Arterial Spin Labelling Technique in Brain Perfusion Imaging. Contrast Media Mol Imaging. 2018; 2018:15. https://doi.org/10.1155/2018/5360375

122. Aslan S, Xu F, Wang PL, Uh J, Yezhuvath US, van Osch M, et al. Estimation of labeling efficiency in pseudocontinuous arterial spin labeling. Magnetic resonance in medicine. 2010; 63(3):765–771. https://doi.org/10.1002/mrm.22245 PMID: 20187183

123. Luh WM, Talagala SL, Li TQ, Bandettini PA. Pseudo-continuous arterial spin labeling at 7 T for human brain: estimation and correction for off-resonance effects using a Prescan. Magn Reson Med. 2013; 69(22488568):402–410. https://doi.org/10.1002/mrm.24266

124. Mora Álvarez MG, Stobbe RW, Beaulieu C. High resolution continuous arterial spin labeling of human cerebral perfusion using a separate neck tagging RF coil. PLOS ONE. 2019; 14(4). https://doi.org/10.1371/journal.pone.0215998 PMID: 31022257

125. Bernier M, Cunnane SC, Whittingstall K. The morphology of the human cerebrovascular system. Human Brain Mapping. 2018; 39(12):4962–4975. https://doi.org/10.1002/hbm.24337